INORGANIC CHEMISTRY

FRONTIERS

Accepted Manuscript

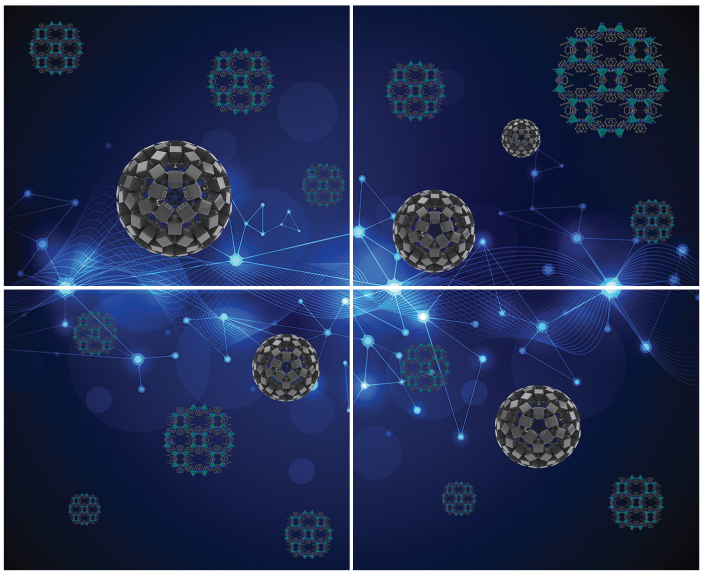

This article can be cited before page numbers have been issued, to do this please use: H. Zhong, Q. Guan, S. You, Z. Wu, H. Ye, L. Xu, Y. Geng, C. Ji, H. Li, C. Zhang, C. Qu and J. Luo, *Inorg. Chem. Front.*, 2026, DOI: 10.1039/D5QI01640A.

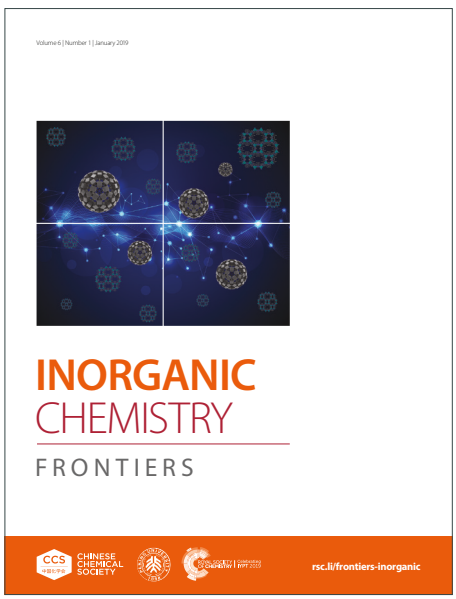

View Article Online
DOI: 10.1039/D5QI01640A

ARTICLE

Aromatic Diamine Constructed Lead-Free Polar Perovskite Towards Stable Self-Driven X-Ray Detection

Received 00th January 20xx,
Accepted 00th January 20xx

DOI: 10.1039/x0xx00000x

Haiqing Zhong, [a, c] Qianwen Guan, [a, b] Shihai You, [d] Zhenyue Wu, [a, b] Huang Ye, [a, b] Lijun Xu, [a, b] Yaru Geng, [a, b] Chengmin Ji, [a, b] Hang Li, [a, b] Chengshu Zhang, [a, b] Chang Qu, [a, b] and Junhua Luo *[a, b, c]

The zero-dimensional (0D) bismuth halide perovskites are attractive candidate semiconductors for X-ray detection due to their low biotoxicity and inhibited ionic migration. However, achieving stable X-ray detection applications of 0D perovskites remains challenging. Introducing aromatic diamine cations into perovskites can enhance structural stability and improve charge transport behaviors. Herein, utilizing the strong anchoring effect of the diamine with the inorganic skeleton, stable X-ray detection is obtained by synthesizing novel 0D polar perovskites, namely AP_2BiI_7 (AP = 4-amidinopyridine). In particular, leveraging intrinsic spontaneous electric polarization that produces a significant 1.15 V photovoltage, the device achieves excellent self-driven X-ray detection at zero electric field, with a high sensitivity of 58 μC Gy^{-1} cm^{-2} and a low detection limit of 100 nGy s^{-1}. Furthermore, the detector exhibits low baseline drift and highly stable X-ray detection, benefiting from the anchoring effect of the aromatic diamine cations in the compound. Our work represents a significant step toward realizing stable, eco-friendly, self-powered X-ray detectors based on perovskite materials.

Introduction

Direct X-ray detection technology converts X-ray photons directly into electrical signals and is widely used in medical imaging, scientific research, industrial inspection, and other fields.[1-5] Halide perovskites, with their high mobility-lifetime product, strong X-ray absorption, and simple synthesis, show great promise for direct X-ray detection due to these excellent optoelectronic properties.[6-9] $MAPbI_3$-based (MA = methylamine) direct X-ray detectors, for instance, achieve sensitivities as high as 2.2 × 10^8 μC Gy^{-1} cm^{-2} and detection limits down to 0.1 nGy s^{-1}.[10, 11] However, the device instability due to severe ionic migration remains a significant challenge for the real application of perovskite detectors.[12, 13, 14] Furthermore, equipment instability could lead to toxic lead leaking from Pb-based perovskites, resulting in significant contamination of soil and groundwater resources.[15, 16] Therefore, developing "green" lead-free perovskites for stable X-ray detection is urgent.

Bismuth ions (Bi^{3+}) share similarities in electronic structure, ionic radius, and electronegativity with lead ions (Pb^{2+}). Despite the difference in charge, these similarities make bismuth a promising, less-toxic alternative to lead in many applications.[17, 18] Bismuth halide perovskites (BHPs) have garnered attention for their large resistivity and low ionic mobility, properties associated with enhanced stability.[19, 20] For example, Liu and his colleagues synthesised a classical 0D BHP, $MA_3Bi_2I_9$, from aliphatic amine cations.[12] Aromatic amine cations are more polar than their aliphatic counterparts, which enhances electronic coupling between inorganic octahedra. This reduces quantum confinement and improves charge transport.[21] More recently, aromatic diamine-constructed BHPs can further effectively enhance the stability of materials and inhibit ionic migration due to the anchoring effect of aromatic diamine cations.[22-24] Yang et al. constructed BHPs (3-(aminomethyl)pyridine)BiI_5 using aromatic diamine cations. The material achieved efficient charge transfer and suppressed ion migration, which ultimately led to stable photodetection performance.[25] However, most currently known BHPs constructed from aromatic diamines lack polar space group symmetry in their crystalline structure. This necessitates the application of an external electric field to achieve efficient charge carrier separation and transport[12, 26], resulting in complex device architectures and significant energy consumption.[27] Therefore, achieving stable self-powered X-ray detection in BHPs constructed with aromatic diamines is essential.

In this work, by introducing aromatic diamine AP^{2+} (AP = 4-amidinopyridine), we have successfully synthesized new polar 0D BHPs, AP_2BiI_7. Anchoring aromatic diamines via both termini to an inorganic framework enhances stability and charge carrier mobility in self-driving detection. Moreover, the device based on polar AP_2BiI_7 exhibits a strong bulk photovoltaic effect (BPVE) with a photovoltage of 1.15 V due to the excellent spontaneous polarization exhibited along the polar *c*-axis of 35.53 μC cm^{-2}. Under zero applied electric field utilizing the BPVE, the detector demonstrates a high sensitivity (58 μC Gy^{-1}cm^{-2}) and a low detection limit (100 nGy s^{-1}). Moreover, the aromatic diamine cation promotes the stability of the AP_2BiI_7; thus, the detector shows a low I_{drift} of 3.8 × 10^{-7} nA cm^{-1} s^{-1} V^{-1} at a 500 V cm^{-1} and demonstrates excellent environmental stability. Our work provides new insights into

[a]State Key Laboratory of Functional Crystals and Devices, Fujian Institute of Research on the Structure of Matter, Chinese Academy of Sciences, Fuzhou, Fujian, 350002, P. R. China
E-mail: jhluo@fjirsm.ac.cn
[b]State Key Laboratory of Structural Chemistry, Fujian Institute of Research on the Structure of Matter, Chinese Academy of Sciences, Fuzhou, Fujian, 350002, P. R. China
[c]College of Chemistry, Fuzhou University, Fuzhou, Fujian, 350108, China
[d]Research Institute of Frontier Science, Southwest Jiaotong University Chengdu, Sichuan 610031, P. R. China

View Article Online
DOI: 10.1039/D5QI01640A

exploring novel 0D bismuth halide perovskite materials for stable self-driven X-ray detection.

Results and discussion

Single-crystal X-ray diffraction (SCXRD) at 300 K confirmed the structure of AP_2BiI_7, which reveals AP_2BiI_7 adopts the *Cc* polar space group (a = 14.2687 Å, b = 14.3448 Å, c = 15.7364 Å) (Table S1). The polar structure exhibits a significant spontaneous polarization along the *c*-axis direction, with calculated polarization values from the point charge model reaching 35.53 μC cm^{-2} (Figure S1 and Table S2). It is therefore promising to observe the obvious bulk photovoltaic effect in the *c*-axis direction. The second harmonic generation signal of AP_2BiI_7 powders is measured to be about 0.11 times that of KH_2PO_4 (KDP), further confirming the non-centrosymmetric structure of AP_2BiI_7 (Figure S2). The structure contains the inorganic $[BiI_6]^{3-}$ octahedron and isolated I^- anion, which are charge-balanced by two independent aromatic diamine AP^{2+}cations, forming a 0D structure (Figure 1a). The Bi-I bond lengths in the inorganic skeleton range from 3.0249(10) Å to 3.1590(10) Å, and the I-Bi-I angles from 83.12(3) to 97.18°(3) (Tables S3 and S4).

The degree of octahedral distortion of AP_2BiI_7 was quantified using the following equation to calculate the distortion index (Δd) and the bond angle variance (σ^2):[28]

$$d = \frac{1}{n}\sum_{i=1}^{n}\left(\frac{d_i - d}{d}\right)^2 \quad (1)$$

$$\sigma^2 = \frac{1}{11}\sum_{n=1}^{12}(\theta_n - 90°)^2 \quad (2)$$

In which the variable d_i (or d) is the individual (or mean) Bi-I bond length, while ϑ_n denotes the bond angle between neighboring Bi-Br bonds. The Δd = 1.64 × 10^{-4}, σ^2 = 20.4 deg^2 have been calculated. It indicates that the AP_2BiI_7 SC structure has minor structural distortion, which facilitates carrier transport. Furthermore, the AP^{2+} molecule bridges and stabilizes the inorganic framework via hydrogen bonds, shortening inter-octahedra distances and suppressing ion migration. The distance between neighboring inorganic skeletons is shorter than that constructed from monoamines. The shortest I-I distance between adjacent $[BiI_6]^{3-}$ octahedrons of AP_2BiI_7 is 4.072 Å, which is shorter than those in $(PBA)_4BiI_7{\cdot}H_2O$ (6.998 Å, PBA = $C_6H_5(CH_2)_4NH_3^+$),[29] $MA_3Bi_2I_9$ (4.57 Å), and BZA_3BiI_6 (4.195Å, BZA = benzylamine).[30] Furthermore, as demonstrated by the Hirschfeld surface analysis, there is a notable molecular electrostatic interaction between the electron-rich I^- anions and the benzene ring ($I^-\cdots\pi$). This interaction is attributed to the proximate distance between the I^- anion and the neighboring benzene ring, which is approximately 3.7 Å (Figure 1b, c, d, and Figure S3).

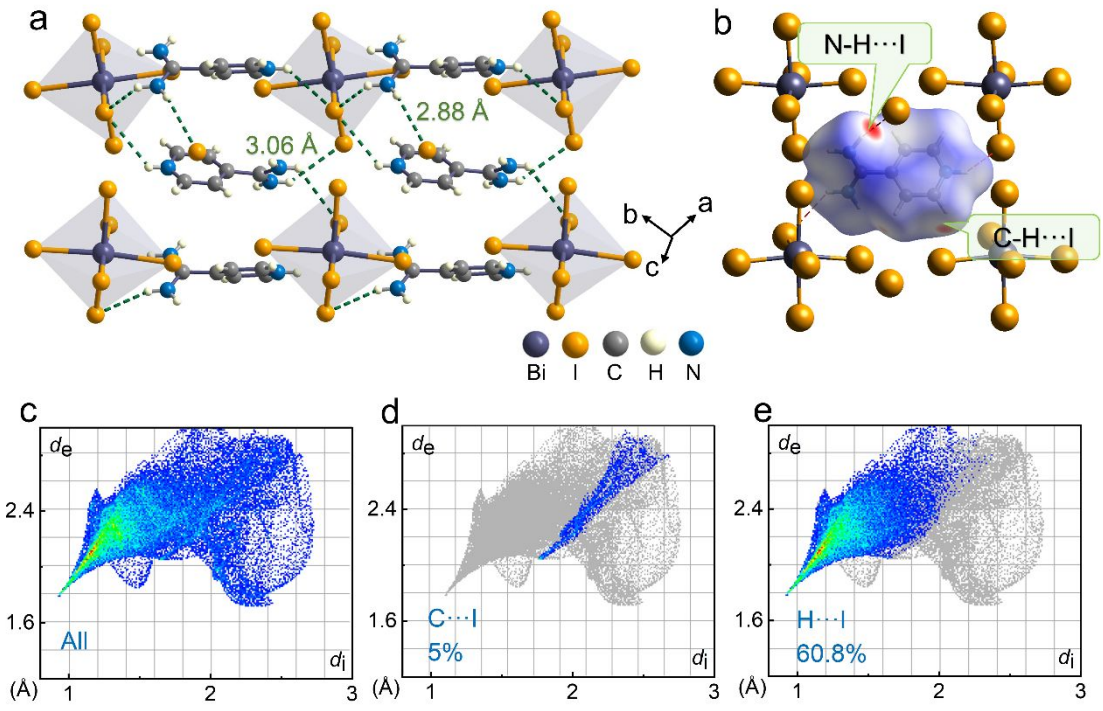

Figure 1. a) The crystal structure of AP_2BiI_7, in which N-H···I hydrogen bonds between aromatic diamine AP^{2+} cations and inorganic skeletons are connected by a dotted line. b) The Hirshfeld d_{norm} surfaces (Since the distance between the atoms is less than the sum of their van der Waals radii, the red regions on the Hirshfeld surface indicate a closer interaction between them.) of the aromatic diamine AP^{2+} and c-e) corresponding 2D fingerprint plots for C···I and H···I contacts in AP_2BiI_7 structure.

The Hirshfeld surface analysis reveals that strong N-H···I hydrogen bonds between the AP^{2+} cations and the inorganic framework account for 60.8% of the total interactions. The account of AP_2BiI_7 indicates strong hydrogen bonding between aromatic

View Article Online
DOI: 10.1039/D5QI01640A

diamine cations (AP^{2+}) and the inorganic skeleton. The stronger hydrogen bonding reduces the distance of adjacent $[BiI_6]^{3-}$-octahedra and promotes lattice rigidity and charge transport, resulting in good photoelectric properties.

Red SC of AP_2BiI_7 with around 5.2 × 4 × 2 mm^3 was grown from the stoichiometric reaction of Bi_2O_3 and AP in a hot hydriodic acid solution via the slow temperature-cooling process (Figure 2a). *PXRD* patterns confirm their phase purity (Figure S4). Meanwhile, the morphology of AP_2BiI_7 was simulated by Mercury software, which matched the obtained bulk SCs and determined the *c*-axis orientation (Figure S5). Additionally, a d_{33} value of 4.9 pC N^{-1} characterizes the clear piezoelectric response observed along the *c*-axis in AP_2BiI_7 crystals (Figure S6). Thus, it is further verified that the AP_2BiI_7 is polar. Furthermore, the *AFM* image of the AP_2BiI_7 crystal surface revealed that it was very smooth and flat with few imperfections. The mean roughness and root-mean-square roughness were found to be 0.235 and 0.304 nm, respectively, thereby confirming the exceptional quality of the crystals referring to Figure 2b. The high quality of AP_2BiI_7 SCs is conducive to excellent carrier transport. Internal crystal defects were further assessed by measuring trap density (n_{trap}) in AP_2BiI_7 SCs with the space-charge-limited current (SCLC) technique.

The current-voltage (*I-V*) curve is subdivided into three distinct regions, as illustrated in Figure 2c**.** These are Trap Filling Limited (TFL) (n > 3), Ohmic (n = 1), and Child (n = 2). The n_{trap} value is calculated using the following equation,[31]

$$n_{trap} = \frac{2\varepsilon\varepsilon_0 V_{TEL}}{eL^2} (3)$$

where V_{TFL} is the threshold voltage, ε_0 represents the vacuum dielectric constant, *e* denotes the unit charge, ε designates the relative dielectric constant, and the variable *L* indicates the length of the conductive channel. The n_{trap} of AP_2BiI_7 is calculated as 3.77 × 10^9 cm^{-3}. The value is comparable to high-quality $MA_3Bi_2I_9$ (1.2 × 10^{10} cm^{-3})[12] and (3-AMP)BiI_5 (3.53 × 10^9 cm^{-3}, 3-AMP = 3-(aminomethyl)pyridine)[32] (for full data, see Table S5). The low n_{trap} will favor charge transport and thus improve the mobility-lifetime ($\mu\tau$) product of AP_2BiI_7. Moreover, the hole-only carrier mobility (μ), determined from the Child region using the Mott–Gurney power law:[33, 34]

$$\mu = \frac{8JL^3}{9\epsilon\epsilon_0 V^2}$$

where *J*, *L* and *V* refer to the dark current density, thickness and applied voltage, respectively. The μ value of AP_2BiI_7 was calculated to be 0.4 cm^2 V^{-1} s^{-1}, which is higher than that of the bismuth-based perovskites such as $Cs_2AgBiBr_6$ (0.05 cm^2 V^{-1} s^{-1}) [35] and $FA_3Bi_2I_9$ (0.0089 cm^2 V^{-1} s^{-1}),[26] indicating that AP_2BiI_7 has excellent charge transport properties. Furthermore, the bulk resistivity (ρ) of AP_2BiI_7 SCs is measured to be 3.55 × 10^{10} Ω cm by fitting the current-voltage curve along *c*-axis (Figure S7), which is comparable to $MA_3Bi_2I_9$ (3.74 × 10^{10} Ω cm),[12] $FA_3Bi_2I_9$ (7.8 × 10^{10} Ω cm, FA = fomamidinium),[26] and $AG_3Bi_2I_9$ (3.78 × 10^{10} Ω cm, AG = aminoguanidinium).[36] Therefore, AP_2BiI_7 with large resistivity is more capable of suppressing dark current, which contributes to improving X-ray detection performance. We have tested the absorption spectra of AP_2BiI_7 to illustrate its optical properties (Figure S8). The absorption edge of the material is located at ~ 646 nm, and the optical band gap was further calculated by fitting the Tauc equation to be ~ 2.0 eV. Then, we performed density-functional theory (DFT) calculations on AP_2BiI_7 (Figure S9),[37-39] and the results show that the material is characterized by an indirect bandgap. The calculated band gap is 1.928 eV, which is in good agreement with the experimental measurements (2.0 eV) and verifies the accuracy of the calculated model. Partial density of states profiles show that the conduction band minimum (CBM) is mainly contributed by N-2p and C-2p orbitals, while the valence band maximum (VBM) is dominated by I-4p orbitals with contributions from Bi-6p orbitals. Combined with the charge density distributions at VBM and CBM, it can be confirmed that the CBM of the material are dominated by its organic cation, while the VBM is mainly determined by the iodide ions in the inorganic components. To further understand the effect of aromatic diamines on the inhibition of ion migration (as shown in Figure 2d), the activation energy can be obtained from the Nernst–Einstein equation, See support information for more details. The E_a value of this compound is 0.96 eV. This is much larger than that of $FA_3Bi_2I_9$ (0.56 eV)[26] and (TMBD)$BiBr_5$ (0.64 eV, *N*, *N*, *N*′, *N*′-tetramethyl-1,4-butanediammonium).[40] It implies that the strong contact between the diamine cations and the inorganic skeletons is useful in increasing the energy barrier for ion migration, and ion migration is effectively suppressed.

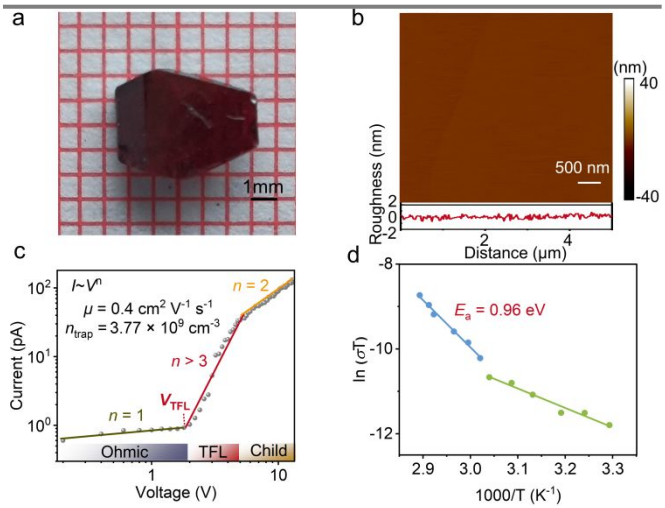

Figure 2. a) An image of a SC of AP_2BiI_7. b) The AFM image of the AP_2BiI_7 crystal. c) The *I-V* curve of the AP_2BiI_7 crystal was obtained using the SCLC method. d) The conductivity of AP_2BiI_7 is temperature-dependent.

View Article Online
DOI: 10.1039/D5QI01640A

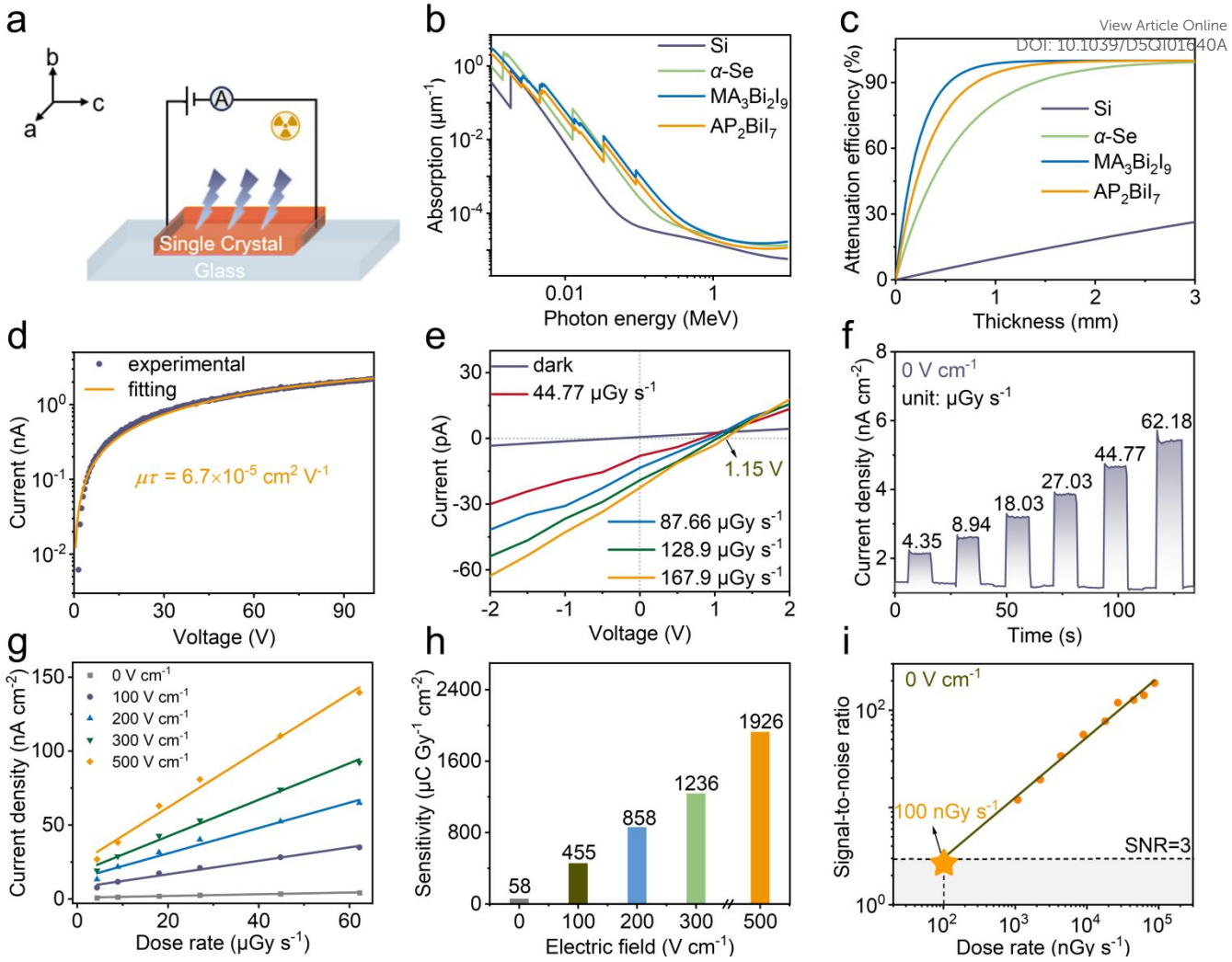

Figure 3. a) Diagram of the AP_2BiI_7 SCs device along the polar *c*-axis direction. b) AP_2BiI_7, Si, *α*-Se, and $MA_3Bi_2I_9$ absorption coefficients as a function of photon energies. c) AP_2BiI_7, Si, *α*-Se, and $MA_3Bi_2I_9$ attenuation efficiency of 50 KeV X-ray photons as a function of thickness. d) The voltage-dependent photocurrent of the AP_2BiI_7 detector yielded a $\mu\tau$ value of 6.7×10^{-5} cm^2 V^{-1} under X-ray irradiation. e) *I-V* traces of the AP_2BiI_7 SC detector in the dark and exposed to X-ray radiation. f) The current density of the AP_2BiI_7 SC detector at 0 V cm^{-1} with increased dose rates. g) The X-ray-induced photocurrent density depends on the dose rate. By fitting the slopes, the sensitivity of the AP_2BiI_7 detector can be determined. h) The sensitivity of the AP_2BiI_7 detector at different electric field. i) The X-ray dose rate-dependent SNR for the AP_2BiI_7 SC detector at 0 V cm^{-1}.

The X-ray performance of AP_2BiI_7 SC was investigated by fabricating it into SC devices. The X-ray device type with an Ag/AP_2BiI_7 SC/Ag two-terminal structure was adopted in Figure 3a and Figure S10. Through the photon cross-section database,[41] we calculate the X-ray absorption spectra of $MA_3Bi_2I_9$, *α*-Se, Si, and AP_2BiI_7 (Figure 3b). The AP_2BiI_7 demonstrates a markedly greater linear absorption coefficient compared to Si. It approaches that of *α*-Se, indicating effective X-ray absorption across a wide photon energy range (1 to 1000 keV) for AP_2BiI_7. Figure 3c shows the attenuation efficiency of AP_2BiI_7 for 50 keV X-ray photons. The AP_2BiI_7 with a thickness of 1mm can absorb approximately 94% of incident photons, which is considerably higher than the ratio (≈ 9.7%) observed for Si. Excellent X-ray attenuation efficiency and efficient charge collection (quantified by $\mu\tau$) are both essential for high-performance detectors. Here, the voltage-dependent photocurrent of AP_2BiI_7 SC detectors can be fitted with the modified Hecht equation to determine the $\mu\tau$ value.

$$I = \frac{I_0 \mu\tau V}{L^2}\left[-\exp\left(-\frac{L^2}{\mu\tau V}\right)\right] \quad (4)$$

Where *L* and *V* represent the electrode spacing and the applied voltage, and I_0 is the saturated photocurrent. The $\mu\tau$ value for AP_2BiI_7, measured at 6.7×10^{-5} cm^2 V^{-1} (Figure 3d), matches the range observed in some BHPs, such as $(R\text{-PPA})_2BiI_5$ (5.6×10^{-5} cm^2 V^{-1}, *R*-PPA = *R*-1-phenylpropylamine)[41] and $(BAH)BiI_4$ (1.95×10^{-4} cm^2 V^{-1}, BAH = benzamidinium),[42] and $(FA)_3Bi_2I_9$ (2.4×10^{-5} cm^2 V^{-1}).[26] The AP_2BiI_7 detector has an enormous potential for X-ray detection, benefiting from its high resistivity, efficient charge collection, and outstanding X-ray absorption. The *I-V* traces of the AP_2BiI_7 detector along the *c*-axis are depicted in Figure 3e, both in the dark and at various X-ray dosage rates. We can observe a significant BPVE of 1.15

View Article Online
DOI: 10.1039/D5QI01604A

V. BPEV originates in the inherent spontaneous polarization of polar crystals. The device is capable of driving the separation and subsequent transport of photogenerated carriers, thereby conferring upon AP_2BiI_7 the ability to perform self-driven detection. Indeed, even at 0 V cm^{-1}, the AP_2BiI_7 detector shows excellent photoresponse (Figure 3f).

Its exceptional response to X-rays is demonstrated by the current density growing linearly from 4.35 to 62.18 μGy s^{-1} as the X-ray dosage rate increases. For comparison, tests were also performed at 100, 200, 300, and 500 V cm^{-1} electric field. (Figure S11). As expected, as the external voltage increases, it is more favorable for carrier collection and therefore higher current densities can be obtained. For AP_2BiI_7 SCs detectors, sensitivity (S) is a key performance index, can be determined by the following formula:[43]

$$S = \frac{(J_{ph} - J_d)}{D} (5)$$

where D is the X-ray dose rate, J_{ph} represents the photocurrent density, and J_d denotes the dark current density. Figure 3g shows that the photocurrent density minus the dark current density (J_{ph}-J_d) is linearly associated with the X-ray dosage rate. By fitting their slopes, the corresponding sensitivities at different electric fields were calculated in Figure 3h. Even in self-driving mode, the sensitivities of AP_2BiI_7 SC detector (58 μC Gy^{-1} cm^{-2}) exceed the commercial a-Se film detector (20 μC Gy^{-1} cm^{-2} @ 10 V μm^{-1}) and 0D monovalent cation BHPs of $(R\text{-PPA})_2BiI_5$ (31 μC Gy^{-1} cm^{-2} @ 0 V).[41] Sensitivities reach 1926 μC Gy^{-1} cm^{-2} at 500 V cm^{-1} as the electric field gradually increased. The value exceeds that of many reported BHPs X-ray detectors (for full data, see Table S6).[44]

Furthermore, it should be noted that as the applied electric field increases, the dark current density also increases. For example, the dark current density under 500 V cm^{-1} is about 37 times that at 0 V cm^{-1}. Self-powered mode reduces dark current, allowing for a lower detection limit. By the definition set forth by the International Union of Pure and Applied Chemistry (IUPAC), the limit of detection (LoD) is defined as a signal-to-noise ratio (SNR) of 3, used to evaluate the detection performance of analytical methods.[45] A LoD of 100 nGy s^{-1} at 0 V cm^{-1} was acquired by calculating the SNR at various dose rates, as seen in Figure 3i, and then fitting the relationship between the SNR and the dose rates. In addition, LoD values were calculated for different electric field as shown in Figure S12. These values significantly reduce the risk of X-ray injury, which is lower than the conventional medical diagnostic LoD of 5.5 μGy s^{-1}.[12, 46]

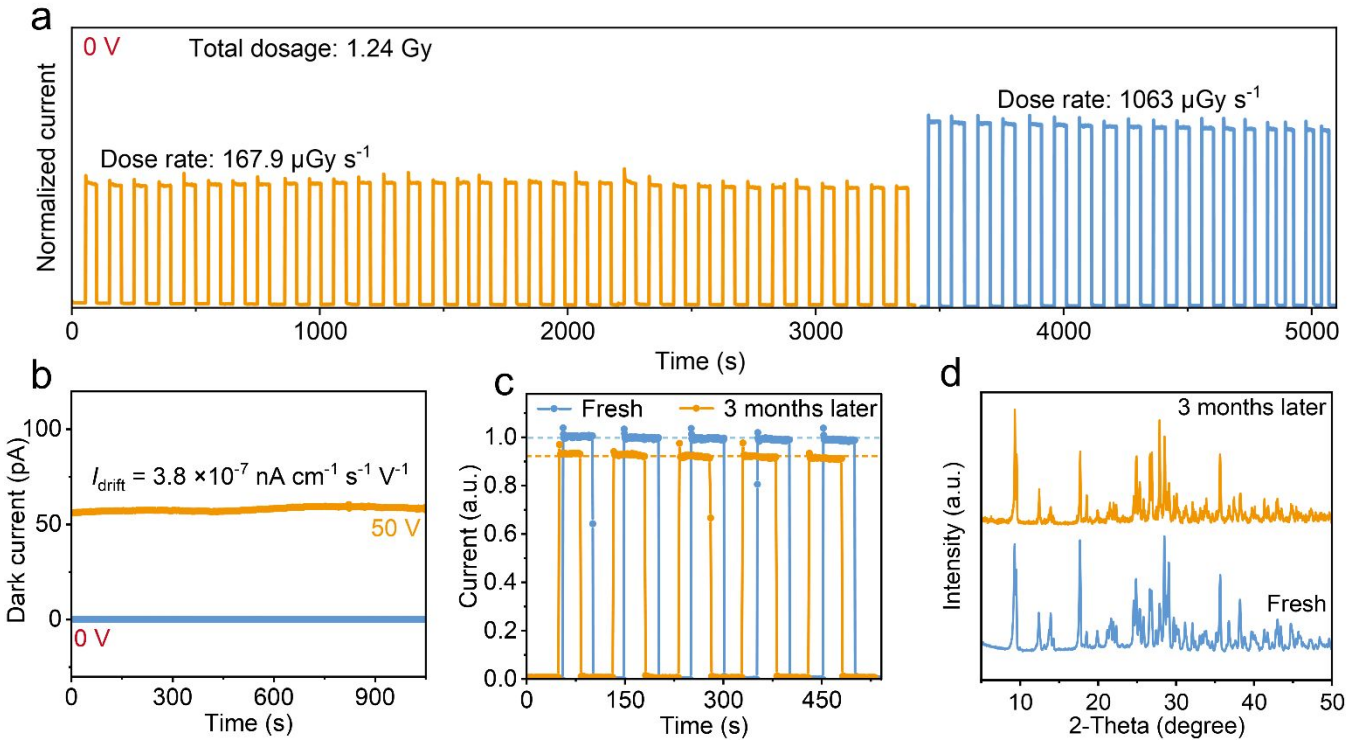

Figure 4. a) X-ray stability test of the unencapsulated AP_2BiI_7 detectors exposed to X-ray irradiation for more than an hour of continuous operation. b) The dark current was measured. c) Initial radiation photoresponse of the AP_2BiI_7 detector at a high dose rate of 1063 μGy s^{-1} and 0 V cm^{-1}, and the radiation photoresponse after three months. d) PXRD patterns of AP_2BiI_7 powders at preparation and after three months.

The stability of equipment is another important performance indicator for its commercialization. The thermogravimetric decomposition temperature of AP_2BiI_7 can reach as high as 563 K, indicating its high thermal stability (Figure S13). It is common to quantify this performance in X-ray detection in terms of radiation stability, I_{drift}, and environmental stability. To evaluate the radiation stability of the device, it was subjected to prolonged, high-dose-rate X-ray irradiation (167.9 μGy s^{-1} and 1063 μGy s^{-1}) at 0 V cm^{-1}. During 5100 s of continuous operation, the photocurrent of AP_2BiI_7 remained stable with a slight decline (Figure 4a), demonstrating the

detector's exceptional operational stability in the self-driven mode. In addition, the AP_2BiI_7 device exhibits excellent radiation stability even at 500 V cm^{-1} (Figure S14). Furtherly, I_{drift} can be obtained from the following equation:[47]

$$I_{\text{drift}} = \frac{(J_t - J_0)}{Et} (6)$$

where J_0 and J_t are the dark current density at the subsequent and initial times, respectively, while E represents the electric field. As is depicted in Figure 4b, the AP_2BiI_7 SC detector not only obtains a markedly stable dark current at 0 V cm^{-1} but also demonstrates an I_{drift} value of 3.8×10^{-7} nA cm^{-1} s^{-1} V^{-1} for the AP_2BiI_7 SC device even under 500 V cm^{-1}. The value is considerably lower than that of previously reported BHPs X-ray devices (Table S6).[48] This contrast again emphasizes the stability advantage of aromatic diamine structures. Finally, the stability in resisting ambient air of the device was investigated. As shown in Figure 4c, after 90 days at a temperature of (24 ± 2) °C and a humidity of (52 ± 10) %, the unencapsulated detector maintains a very high level of operational stability, with only a slight degradation of the X-ray photoresponse (approximately reduced to 92% of the original). In addition, the unencapsulated device retained approximately 90% of its sensitivity after 90 days (Figure S15). The result demonstrates a level of environmental stability in the material system we developed. Furthermore, the AP_2BiI_7 still maintains excellent phase stability by *PXRD* after three months (Figure 4d). These indicate the superior environmental stability of the AP_2BiI_7 SC device. Such stability and exceptional self-driven X-ray detection performance exhibit the great commercial application prospect of AP_2BiI_7 perovskite devices.

Conclusions

In summary, a novel 0D lead-free polar perovskite, AP_2BiI_7, was synthesized by incorporating aromatic diamine AP^{2+} cations. High-quality SCs of AP_2BiI_7 exhibit a lower trap density n_{trap} (3.77×10^9 cm^{-3}) and a high resistivity (3.55×10^{10} cm^{-3}). Aromatic diamines AP^{2+} with anchoring effect can effectively improve stability and charge transport behaviors. Moreover, such a polar structure thus gives them intrinsic spontaneous polarization along the polar axis direction, which further results in a strong BPVE with a photovoltage of 1.15 V under X-ray irradiation. It acts as the driving force for separating and transporting the X-ray-generated charge carriers, thereby endowing AP_2BiI_7 with the capability for self-driven detection. By leveraging the bulk photovoltage as the driving force, the 0D AP_2BiI_7 detector exhibits a notable sensitivity of 58 μC Gy^{-1} cm^{-2} and a low LoD of 100 nGy s^{-1} at 0V cm^{-1}. Moreover, the aromatic diamine cation through the strong anchoring effect gives AP_2BiI_7 a stable structure, which makes AP_2BiI_7 show a low I_{drift} of 3.8×10^{-7} nA cm^{-1} s^{-1} V^{-1} under 500 V cm^{-1}, as well as excellent radiative stability both under self-drive mode and applied electric field. Impressively, even after three months, the AP_2BiI_7 shows excellent environmental stability with only a slight decrease in photoresponse. This work demonstrates the first self-driven X-ray detection in 0D aromatic diamine-based BHPs, offering new insights for designing "green" and stable self-driven radiation detectors based on hybrid perovskites.

Author contributions

H. Q. Zhong prepared the samples and wrote the manuscript. C. Qu, G. R. Chen, H. W. Yang, and Y. Wang performed the photoelectric properties. S. H. You, Z. Y. Wu, H. Ye, L. J. Xu, Y. R. Geng, H. Li, and C. S. Zhang provided suggestions for the project. Q. W. Guan and J. H. Luo designed and directed this project. All the authors discussed and commented on the manuscript. CRediT: Haiqing Zhong data curation, formal analysis, investigation, visualization, writing-original draft; Qianwen Guan writing-review & editing; Shihai You data curation, formal analysis; Zhenyue Wu data curation, formal analysis; Huang Ye data curation, formal analysis; Lijun Xu data curation; Yaru Geng data curation, formal analysis; Chengmin Ji data curation; Hang Li data curation; Chengshu Zhang data curation; Chang Qu data curation; Junhua Luo formal analysis, funding acquisition, project administration, supervision, writing-review & editing.

Conflict of Interest

There are no conflicts to declare.

Data availability

The data that support the findings of this study are available in the Supporting Information of this article. The crystallographic data have been deposited at the Cambridge Crystallographic Data Centre (CCDC) under deposition number 2401299. These data can be obtained free of charge from www.ccdc.cam.ac.uk/data_request/cif.

Acknowledgements

This work was financially supported by the National Natural Science Foundation of China (22435005, 22193042, 21921001, 22125110, 22122507, and U21A2069), the Key Research Program of Frontier Sciences of the Chinese Academy of Sciences (ZDBS-LY-SLH024).

References

1. Y. C. Kim, K. H. Kim, D.-Y. Son, D.-N. Jeong, J.-Y. Seo, Y. S. Choi, I. T. Han, S. Y. Lee and N.-G. Park, Printable organometallic perovskite enables large-area, low-dose X-ray imaging, *Nature*, 2017, **550**, 87-91.
2. J. Zhao, L. Zhao, Y. Deng, X. Xiao, Z. Ni, S. Xu and J. Huang, Perovskite-filled membranes for flexible and large-area direct-conversion X-ray detector arrays, *Nat. Photonics*, 2020, **14**, 612-617.
3. H. Wu, Y. Ge, G. Niu and J. Tang, Metal Halide Perovskites for X-Ray Detection and Imaging, *Matter*, 2021, **4**, 144-163.
4. Q. Chen, J. Wu, X. Ou, B. Huang, J. Almutlaq, A. A. Zhumekenov, X. Guan, S. Han, L. Liang, Z. Yi, J. Li, X. Xie, Y. Wang, Y. Li, D. Fan, D. B. L. Teh, A. H. All, O. F. Mohammed, O. M. Bakr, T. Wu, M. Bettinelli, H. Yang, W. Huang and X. Liu, All-inorganic perovskite nanocrystal scintillators, *Nature*, 2018, **561**, 88-93.
5. J. Jiang, M. Xiong, K. Fan, C. Bao, D. Xin, Z. Pan, L. Fei, H. Huang, L. Zhou, K. Yao, X. Zheng, L. Shen and F. Gao, Synergistic strain engineering of perovskite single crystals for highly stable and sensitive X-ray detectors with low-bias imaging and monitoring, *Nat. Photonics*, 2022, **16**, 575-581.

6. S. Deumel, A. van Breemen, G. Gelinck, B. Peeters, J. Maas, R. Verbeek, S. Shanmugam, H. Akkerman, E. Meulenkamp, J. E. Huerdler, M. Acharya, M. García-Batlle, O. Almora, A. Guerrero, G. Garcia-Belmonte, W. Heiss, O. Schmidt and S. F. Tedde, High-sensitivity high-resolution X-ray imaging with soft-sintered metal halide perovskites, *Nat. Electron.*, 2021, **4**, 681-688.
7. S. Yakunin, M. Sytnyk, D. Kriegner, S. Shrestha, M. Richter, G. J. Matt, H. Azimi, C. J. Brabec, J. Stangl, M. V. Kovalenko and W. Heiss, Detection of X-ray photons by solution-processed lead halide perovskites, *Nat. Photonics*, 2015, **9**, 444-449.
8. H. Wei, Y. Fang, P. Mulligan, W. Chuirazzi, H.-H. Fang, C. Wang, B. R. Ecker, Y. Gao, M. A. Loi, L. Cao and J. Huang, Sensitive X-ray detectors made of methylammonium lead tribromide perovskite single crystals, *Nat. Photonics*, 2016, **10**, 333-339.
9. Y. Zhou, J. Chen, O. M. Bakr and O. F. Mohammed, Metal Halide Perovskites for X-ray Imaging Scintillators and Detectors, *ACS Energy Lett.*, 2021, **6**, 739-768.
10. Y. Song, L. Li, M. Hao, W. Bi, A. Wang, Y. Kang, H. Li, X. Li, Y. Fang, D. Yang and Q. Dong, Elimination of Interfacial‐Electrochemical‐Reaction‐Induced Polarization in Perovskite Single Crystals for Ultrasensitive and Stable X‐Ray Detector Arrays, *Adv. Mater.*, 2021, **33**, 2103078.
11. A. Glushkova, P. Andričević, R. Smajda, B. Náfrádi, M. Kollár, V. Djokić, A. Arakcheeva, L. Forró, R. Pugin and E. Horváth, Ultrasensitive 3D Aerosol-Jet-Printed Perovskite X-ray Photodetector, *ACS Nano*, 2021, **15**, 4077-4084.
12. Y. Liu, Z. Xu, Z. Yang, Y. Zhang, J. Cui, Y. He, H. Ye, K. Zhao, H. Sun, R. Lu, M. Liu, M. G. Kanatzidis and S. Liu, Inch-Size 0D-Structured Lead-Free Perovskite Single Crystals for Highly Sensitive Stable X-Ray Imaging, *Matter*, 2020, **3**, 180-196.
13. A. Fakharuddin, U. Shabbir, W. Qiu, T. Iqbal, M. Sultan, P. Heremans and L. Schmidt-Mende, Inorganic and Layered Perovskites for Optoelectronic Devices, *Adv. Mater.*, 2019, **31**, 1807095.
14. X. Feng, L. Zhang, X. Feng, J. You, J. Pi, H. Zeng, D. Chu, C. Xue, K. Zhao, S. Jia, P. Tong, Z. Jin, Y. Liu, A. K. Y. Jen and S. F. Liu, Ion Migration Suppression via Doping Multivalent Cations in Perovskite for High Thermal Stability X-ray Detectors, *ACS Energy Lett.*, 2025, **10**, 685-695.
15. C.-H. Chen, S.-N. Cheng, L. Cheng, Z.-K. Wang and L.-S. Liao, Toxicity, Leakage, and Recycling of Lead in Perovskite Photovoltaics, *Adv. Energy Mater.*, 2023, **13**, 2204144.
16. X. Xiao, M. Wang, S. Chen, Y. Zhang, H. Gu, Y. Deng, G. Yang, C. Fei, B. Chen, Y. Lin, M. D. Dickey and J. Huang, Lead-adsorbing ionogel-based encapsulation for impact-resistant, stable, and lead-safe perovskite modules, *Sci. Adv.*, **7**, eabi8249.
17. R. Zhuang, X. Wang, W. Ma, Y. Wu, X. Chen, L. Tang, H. Zhu, J. Liu, L. Wu, W. Zhou, X. Liu and Y. Yang, Highly sensitive X-ray detector made of layered perovskite-like $(NH_4)_3Bi_2I_9$ single crystal with anisotropic response, *Nat. Photonics*, 2019, **13**, 602-608.
18. C. Wu, Q. Zhang, G. Liu, Z. Zhang, D. Wang, B. Qu, Z. Chen and L. Xiao, From Pb to Bi: A Promising Family of Pb‐Free Optoelectronic Materials and Devices, *Adv. Energy Mater.*, 2019, **10**, 1902496.
19. M. Chen, X. Dong, D. Chu, B. Jia, X. Zhang, Z. Zhao, J. Hao, Y. Zhang, J. Feng, X. Ren, Y. Liang, R. Shi, A. Najar, Y. Liu and S. Liu, Interlayer-Spacing Engineering of Lead-Free Perovskite Single Crystal for High-Performance X-Ray Imaging, *Adv. Mater.*, 2023, **35**, 2211977.
20. B. Zhang, Y. Zhang, H. Su, E. Huang, Z. Zhao, Z. Xu, Y. Liu, L. Zhang, Z. Zeng, J. You, A. K. Y. Jen and S. Liu, Rational Design of A-Site Cation for High Performance Lead-Free Perovskite X-Ray Detectors, *Small*, 2024, **20**, 2405071.
21. Y. Shen, S. Hu, Y. Meng, S. Yip and J. C. Ho, Aromatic spacer engineering for 2D halide perovskites and their application in solar cells, *Materials Today Electronics*, 2024, **8**, 100100.
22. X. Li, B. Traoré, M. Kepenekian, L. Li, C. C. Stoumpos, P. Guo, J. Even, C. Katan and M. G. Kanatzidis, Bismuth/Silver-Based Two-Dimensional Iodide Double and One-Dimensional Bi Perovskites: Interplay between Structural and Electronic Dimensions, *Chem. Mater.*, 2021, **33**, 6206-6216.
23. L. Gao, X. Li, B. Traoré, Y. Zhang, J. Fang, Y. Han, J. Even, C. Katan, K. Zhao, S. Liu and M. G. Kanatzidis, m-Phenylenediammonium as a New Spacer for Dion–Jacobson Two-Dimensional Perovskites, *J. Am. Chem. Soc.*, 2021, **143**, 12063-12073.
24. X. Li, W. Ke, B. Traoré, P. Guo, I. Hadar, M. Kepenekian, J. Even, C. Katan, C. C. Stoumpos, R. D. Schaller and M. G. Kanatzidis, Two-Dimensional Dion–Jacobson Hybrid Lead Iodide Perovskites with Aromatic Diammonium Cations, *J. Am. Chem. Soc.*, 2019, **141**, 12880-12890.
25. X. Yang, Y. H. Huang, X. D. Wang, W. G. Li and D. B. Kuang, A‐Site Diamine Cation Anchoring Enables Efficient Charge Transfer and Suppressed Ion Migration in Bi‐Based Hybrid Perovskite Single Crystals, *Angew. Chem. Int. Ed.*, 2022, **61**, e202204663
26. W. Li, D. Xin, S. Tie, J. Ren, S. Dong, L. Lei, X. Zheng, Y. Zhao and W.-H. Zhang, Zero-Dimensional Lead-Free $FA_3Bi_2I_9$ Single Crystals for High-Performance X-ray Detection, *J. Phys. Chem. Lett.*, 2021, **12**, 1778-1785.
27. Z. Zhao, Q. Fan, Y. Liu, H. Rong, H. Ni, L. Wei, X. Zhao, J. Luo and Z. Sun, Lead-Free Bismuth-Based Perovskite X-ray Detector with High Sensitivity and Low Detection Limit, *ACS Appl. Mater. Interfaces*, 2024, **16**, 38283-38289.
28. B. Zhang, T. Zheng, J. You, C. Ma, Y. Liu, L. Zhang, J. Xi, G. Dong, M. Liu and S. Liu, Electron-Phonon Coupling Suppression by Enhanced Lattice Rigidity in 2D Perovskite Single Crystals for High-Performance X-Ray Detection, *Adv. Mater.*, 2023, **35**, 2208875.
29. D. Chen, S. Hao, L. Fan, Y. Guo, J. Yao, C. Wolverton, M. G. Kanatzidis, J. Zhao and Q. Liu, Broad Photoluminescence and Second-Harmonic Generation in the Noncentrosymmetric Organic–Inorganic Hybrid Halide $(C_6H_5(CH_2)_4NH_3)_4MX_7{\cdot}H_2O$ (M = Bi, In, X = Br or I), *Chem. Mater.*, 2021, **33**, 8106-8111.
30. Z.-X. Zhang, C.-Y. Su, J. Li, X.-J. Song, D.-W. Fu and Y. Zhang, Ferroelastic Hybrid Bismuth Bromides with Dual Dielectric Switches, *Chem. Mater.*, 2021, **33**, 5790-5799.
31. Z. Xu, X. Liu, Y. Li, X. Liu, T. Yang, C. Ji, S. Han, Y. Xu, J. Luo and Z. Sun, Exploring Lead-Free Hybrid Double Perovskite Crystals of $(BA)_2CsAgBiBr_7$ with Large Mobility-Lifetime Product toward X-Ray Detection, *Angew. Chem. Int. Ed.*, 2019, **58**, 15757-15761.
32. X. Yang, Y.-H. Huang, X.-D. Wang, W.-G. Li and D.-B. Kuang, A-Site Diamine Cation Anchoring Enables Efficient Charge Transfer and Suppressed Ion Migration in Bi-Based Hybrid

Perovskite Single Crystals, *Angew. Chem. Int. Ed.*, 2022, **61**, e202204663.

33. Y. Huang, L. Qiao, Y. Jiang, T. He, R. Long, F. Yang, L. Wang, X. Lei, M. Yuan and J. Chen, A-site Cation Engineering for Highly Efficient MAPbI3 Single-Crystal X-ray Detector, *Angew. Chem. Int. Ed.*, 2019, **58**, 17834-17842.
34. D. Liu, Y. Zheng, X. Y. Sui, X. F. Wu, C. Zou, Y. Peng, X. Liu, M. Lin, Z. Wei, H. Zhou, Y.-F. Yao, S. Dai, H. Yuan, H. G. Yang, S. Yang and Y. Hou, Universal growth of perovskite thin monocrystals from high solute flux for sensitive self-driven X-ray detection, *Nat. Commun.*, 2024, **15**, 2390.
35. B. Wu, W. Ning, Q. Xu, M. Manjappa, M. Feng, S. Ye, J. Fu, S. Lie, T. Yin, F. Wang, T. W. Goh, P. C. Harikesh, Y. K. E. Tay, Z. X. Shen, F. Huang, R. Singh, G. Zhou, F. Gao and T. C. Sum, Strong self-trapping by deformation potential limits photovoltaic performance in bismuth double perovskite, *Sci. Adv.*, **7**, eabd3160.
36. M. Chen, X. Dong, D. Chu, B. Jia, X. Zhang, Z. Zhao, J. Hao, Y. Zhang, J. Feng, X. Ren, Y. Liang, R. Shi, A. Najar, Y. Liu and S. Liu, Interlayer - Spacing Engineering of Lead - Free Perovskite Single Crystal for High - Performance X - Ray Imaging, *Adv. Mater.*, 2023, **35**, 2211977.
37. S. Zeng, X. Sui, D. Liu, Y. Peng, Q. Li, M. Song, J. Qian, H. Yuan, S. Yang, H. G. Yang and Y. Hou, Molecular Ordering in Low-Dimensional Hybrid Perovskites for Improved X-Ray Detection, *Angew. Chem. Int. Ed.*, 2025, **64**, e202506973.
38. W. Pan, Y. He, W. Li, L. Liu, K. Guo, J. Zhang, C. Wang, B. Li, H. Huang, J. Zhang, B. Yang and H. Wei, Cation-π interactions enabled water-stable perovskite X-ray flat mini-panel imager, *Nat. Commun.*, 2024, **15**, 257.
39. Z. Li, G. Peng, Z. Li, Y. Xu, T. Wang, H. Wang, Z. Liu, G. Wang, L. Ding and Z. Jin, Hydrogen Bonds Strengthened Metal-Free Perovskite for Degradable X-ray Detector with Enhanced Stability, Flexibility and Sensitivity, *Angew. Chem. Int. Ed.*, 2023, **62**, e202218349.
40. Z. Yu, K. Kuang, M. Li, X. Xiao, B. He, S. Cao, J. Tang, Y. He and J. Chen, Lattice Manipulation with Di-Tertiary Ammonium Spacer in Bismuth Bromide Perovskite Directs Efficient Charge Transport and Suppressed Ion Migration for Photodetector Applications, *Small*, 2024, **20**, 2401847.
41. S. You, Z. K. Zhu, S. Dai, J. Wu, Q. Guan, T. Zhu, P. Yu, C. Chen, Q. Chen and J. Luo, Inch - Size Single Crystals of Lead - Free Chiral Perovskites with Bulk Photovoltaic Effect for Stable Self - Driven X - Ray Detection, *Adv. Funct. Mater.*, 2023, **33**, 2303523.
42. C. Ma, H. Li, M. Chen, Y. Liu, K. Zhao and S. Liu, Water - Resistant Lead - Free Perovskitoid Single Crystal for Efficient X - Ray Detection, *Adv. Funct. Mater.*, 2022, **32**, 2202160.
43. W. Pan, H. Wu, J. Luo, Z. Deng, C. Ge, C. Chen, X. Jiang, W.-J. Yin, G. Niu, L. Zhu, L. Yin, Y. Zhou, Q. Xie, X. Ke, M. Sui and J. Tang, $Cs_2AgBiBr_6$ single-crystal X-ray detectors with a low detection limit, *Nat. Photonics*, 2017, **11**, 726-732.
44. Y. Zhang, Y. Liu, Z. Xu, H. Ye, Z. Yang, J. You, M. Liu, Y. He, M. G. Kanatzidis and S. Liu, Nucleation-controlled growth of superior lead-free perovskite $Cs_3Bi_2I_9$ single-crystals for high-performance X-ray detection, *Nat. Commun.*, 2020, **11**, 2304.
45. Z. Li, F. Zhou, H. Yao, Z. Ci, Z. Yang and Z. Jin, Halide perovskites for high-performance X-ray detector, *Mater. Today*, 2021, **48**, 155-175.
46. Z. Li, F. Zhou, H. Yao, Z. Ci, Z. Yang and Z. Jin, Halide perovskites for high-performance X-ray detector, *Mater. Today*, 2021, **48**, 155-175.
47. S. You, P. Yu, T. Zhu, C. Lin, J. Wu, Z. K. Zhu, C. Zhang, Z. Li, C. Ji and J. Luo, Ionizing Radiation Responsive Anomalous Photovoltage Drives Sensitive Self - Powered X - Ray Detection, *Adv. Funct. Mater.*, 2024, **34**, 2310916.
48. J. Wu, S. You, P. Yu, Q. Guan, Z.-K. Zhu, Z. Li, C. Qu, H. Zhong, L. Li and J. Luo, Chirality Inducing Polar Photovoltage in a 2D Lead-Free Double Perovskite toward Self-Powered X-ray Detection, *ACS Energy Lett.*, 2023, **8**, 2809-2816.

View Article Online
DOI: 10.1039/D5QI01640A

The data supporting this article have been included as part of the Supplementary Information. For example, additional computational details and experimental details, materials, and methods, including crystal morphology, crystal structure data, PXRD patterns, the TG curve, and basic photoelectric properties.